ADVANCED FUNCTIONAL MATERIALS

Supporting Information

for *Adv. Funct. Mater.*, DOI: 10.1002/adfm.201806584

Room-Temperature Metallic Fusion-Induced Layer-by-Layer Assembly for Highly Flexible Electrode Applications

Yongkwon Song, Donghee Kim, Sungkun Kang, Younji Ko, Jongkuk Ko, June Huh, Yongmin Ko, Seung Woo Lee, and Jinhan Cho**

Supporting Information

Room-Temperature Metallic Fusion-Induced Layer-by-Layer Assembly for Highly Flexible Electrode Applications

Yongkwon Song, Donghee Kim, Sungkun Kang, Younji Ko, Jongkuk Ko, June Huh, Yongmin Ko, Seung Woo Lee,* and Jinhan Cho*

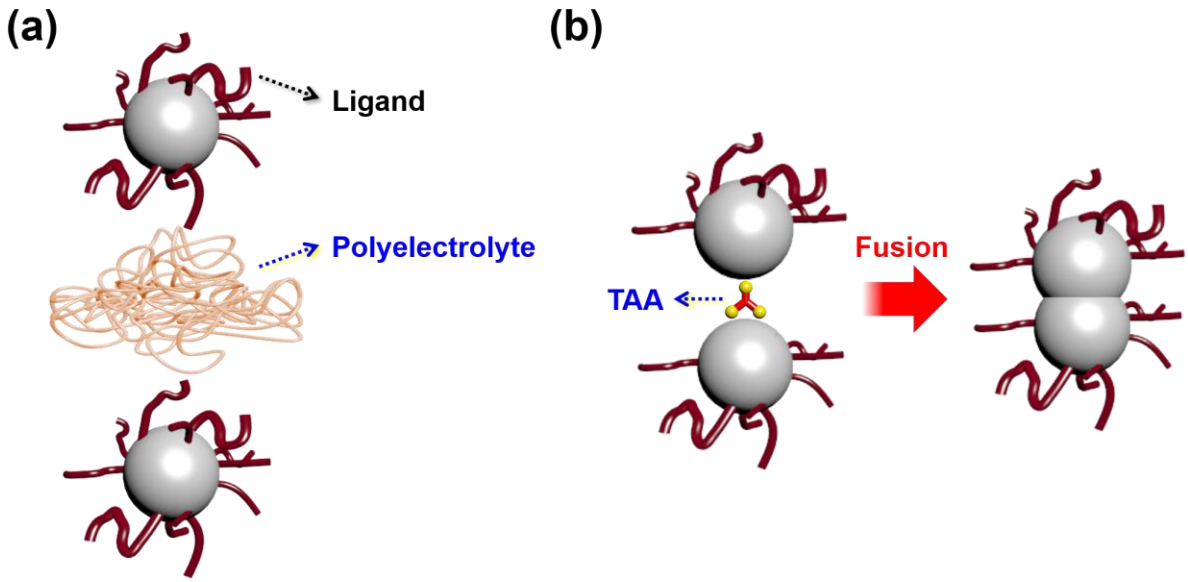

Figure S1. Schematic diagram showing the difference between (a) Charged metal NP/oppositely charged polymer linker using traditional electrostatic LbL assembly and (b) Fused metal NP/small organic linker using our approach.

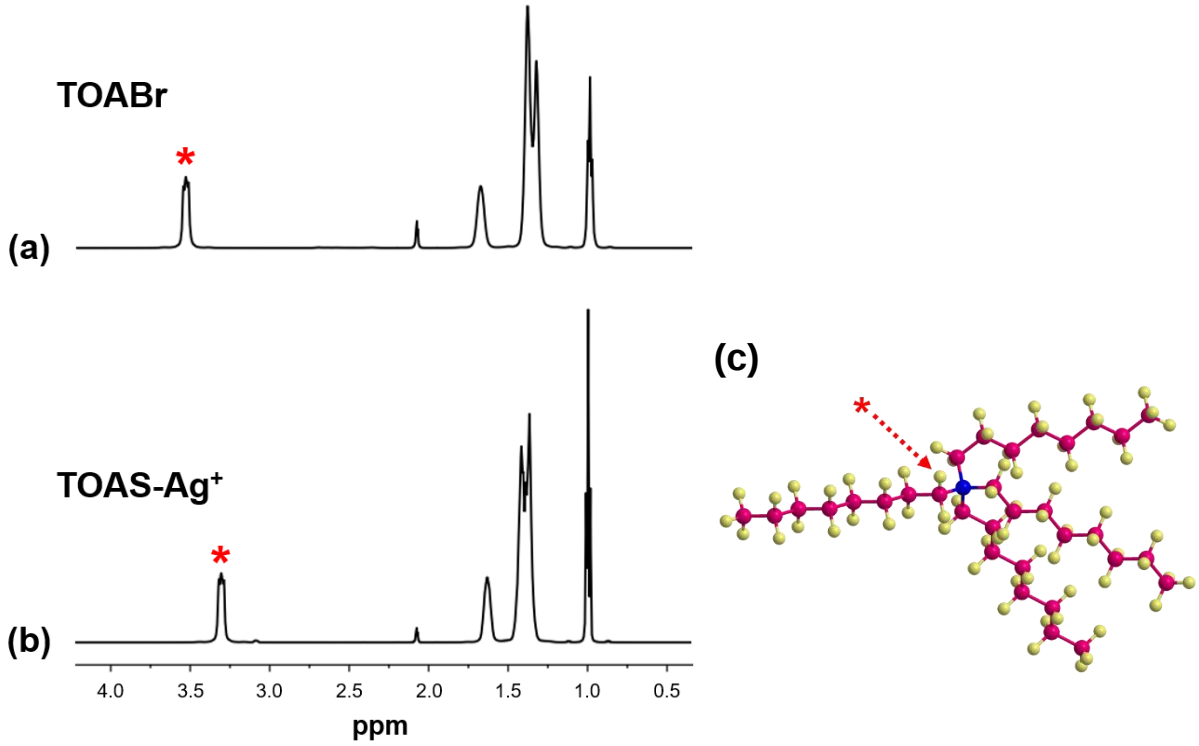

Figure S2. ^{1}H NMR spectra of a) tetraoctylammonium bromide (TOABr) and b) tetraoctylammonium sulfate (TOAS) complexed with precursor silver ions (Ag^{+}). c) Ball-and-stick molecular model of tetraoctylammonium (TOA), where blue, red, and yellow balls indicate nitrogen, carbon, and hydrogen atoms, respectively. The Ag nanoparticles (NPs) were synthesized by the modified Brust−Schiffrin method and their complex structures before reduction were characterized by examining the ^{1}H NMR chemical shifts. a) ^{1}H NMR spectra (500 MHz, toluene-d_8) of the TOABr: δ = 3.54 (2H, broad, NCH_2), 1.67 (2H, broad, NCH$_2$CH_2), 1.38−1.33 (10H, m), 1.00−0.97 ppm (3H, m, CH_3) and b) TOAS: δ = 3.37 (2H, broad, NCH_2), 1.64 (2H, broad, NCH$_2$CH_2), 1.42−1.37 (10H, m), 1.01−0.98 ppm (3H, m, CH_3).[S1] The signals of the first methylenic protons (*) adjacent to the ammonium nitrogen atom were shifted upfield in TOAS relative to those in TOABr, implying the complexation of TOAS ligands and silver ions.

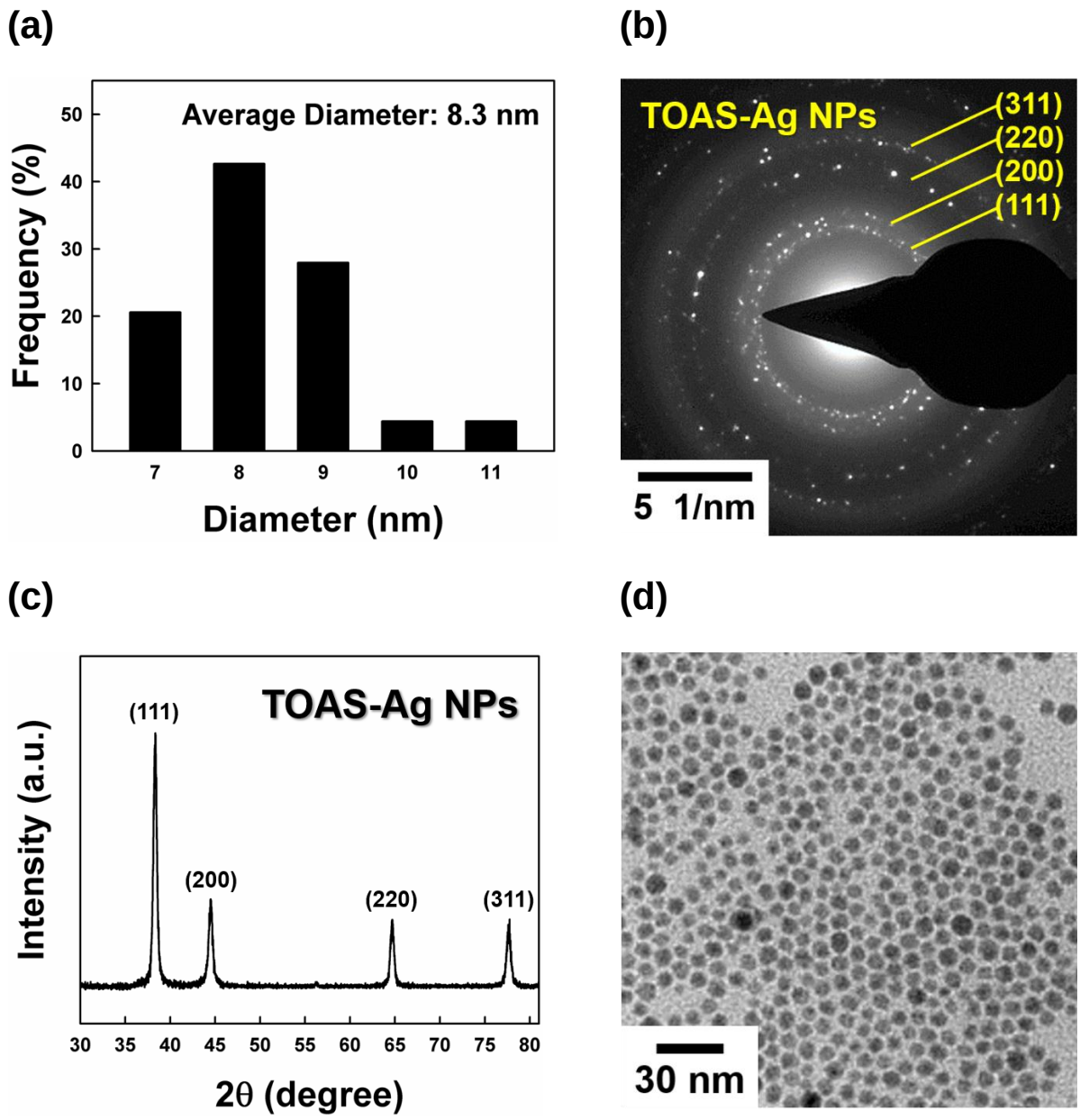

Figure S3. a) Size distribution of TOAS-Ag NPs measured from HR-TEM image. The average diameter of TOAS-Ag NPs was approximately 8.3 nm. b) Selected-area electron diffraction (SAED) pattern and c) X-ray diffraction (XRD) pattern of TOAS-Ag NPs. The XRD pattern is well matched with the face-centered cubic structure of Ag (JCPDS Card No. 01-087-0719). d) HR-TEM image of TOAS-Ag NPs acquired one month after synthesis.

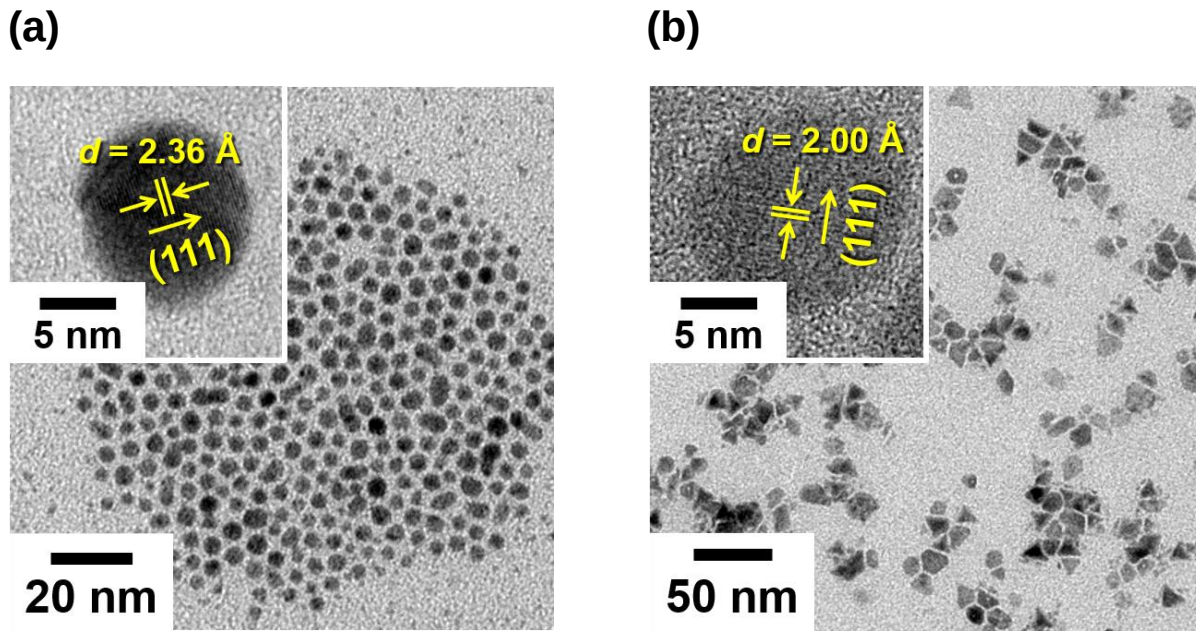

Figure S4. HR-TEM images of TOAS-stabilized a) Au NPs and b) Cu NPs.

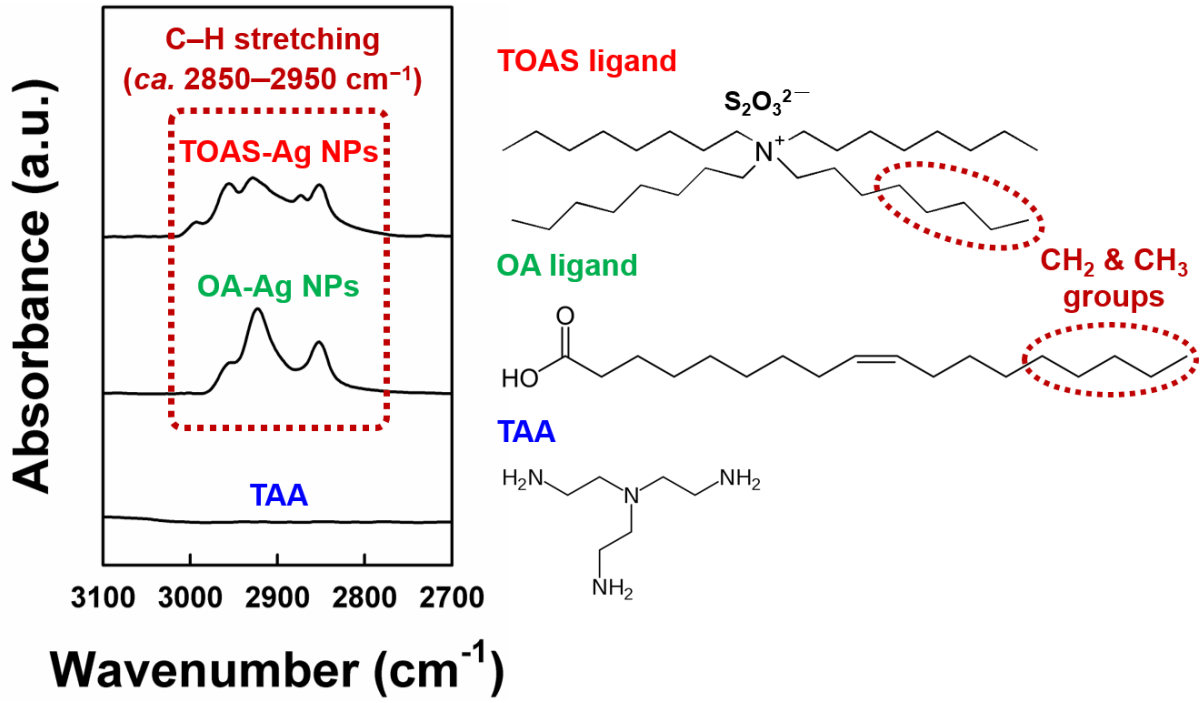

Figure S5. FTIR spectra of TOAS-Ag NPs, OA-Ag NPs, and TAA. TOAS-Ag NPs and OA-Ag NPs showed the C−H stretching peaks derived from the long alkyl chains of ligands in the range from 3000 to 2800 cm^{-1}, whereas TAA did not show any absorbance peak in that range.

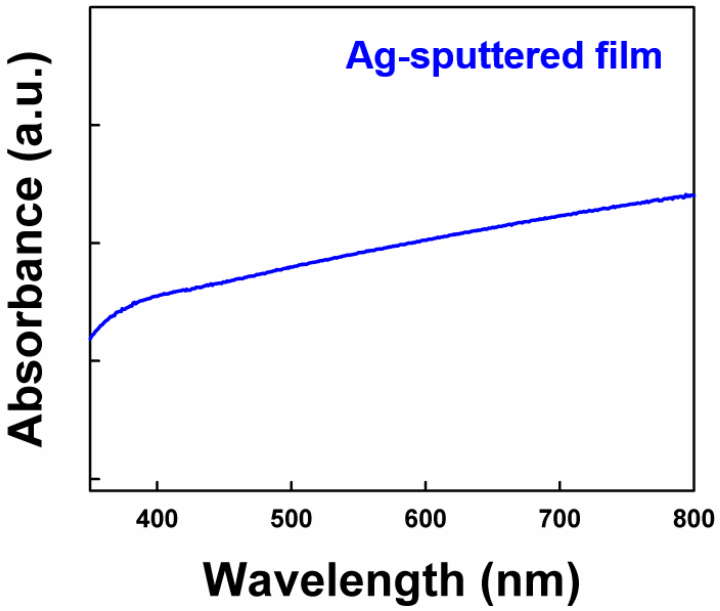

Figure S6. UV-vis absorbance spectrum of Ag-sputtered film.

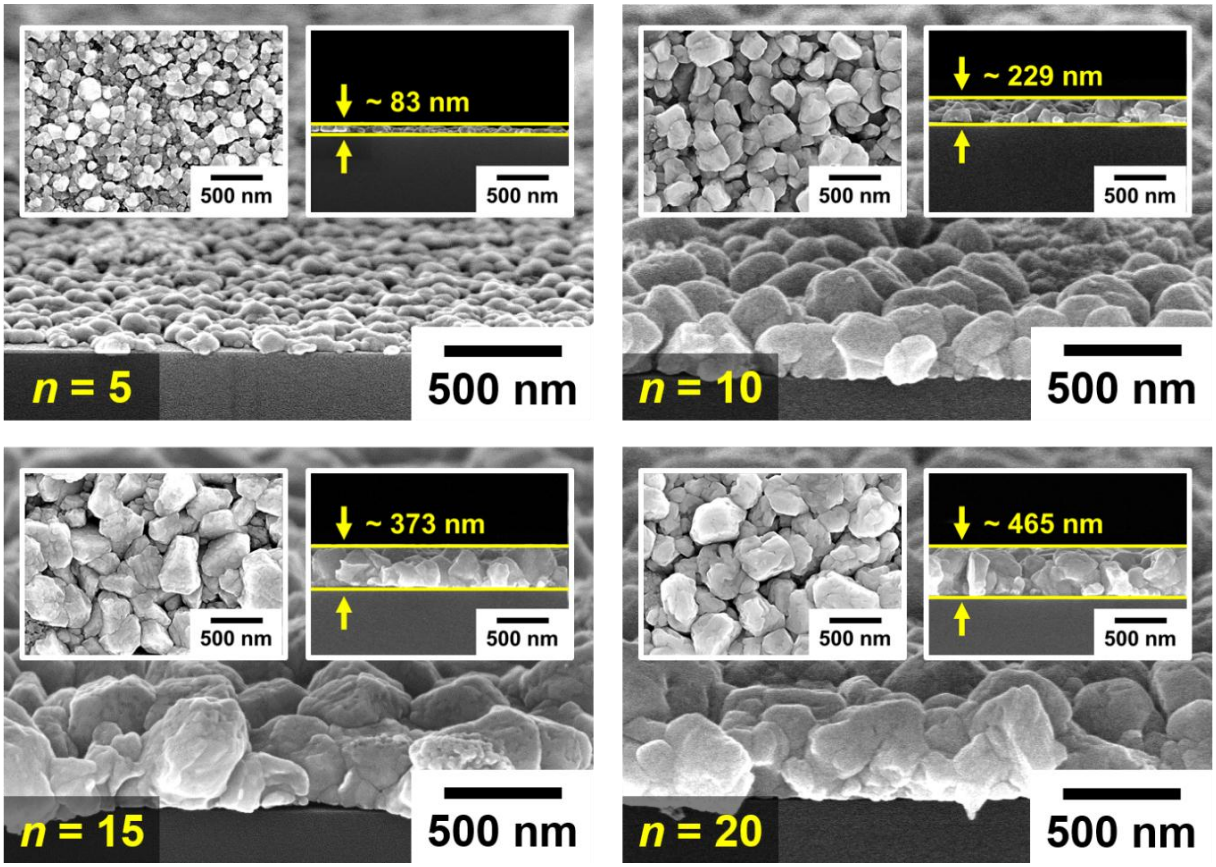

Figure S7. Tilted (main images), cross-sectional (top right insets) and planar (top left insets) FE-SEM images of (TOAS-Ag NP/TAA)$_n$ multilayers on Si wafers as a function of bilayer number (n = 5, 10, 15, and 20).

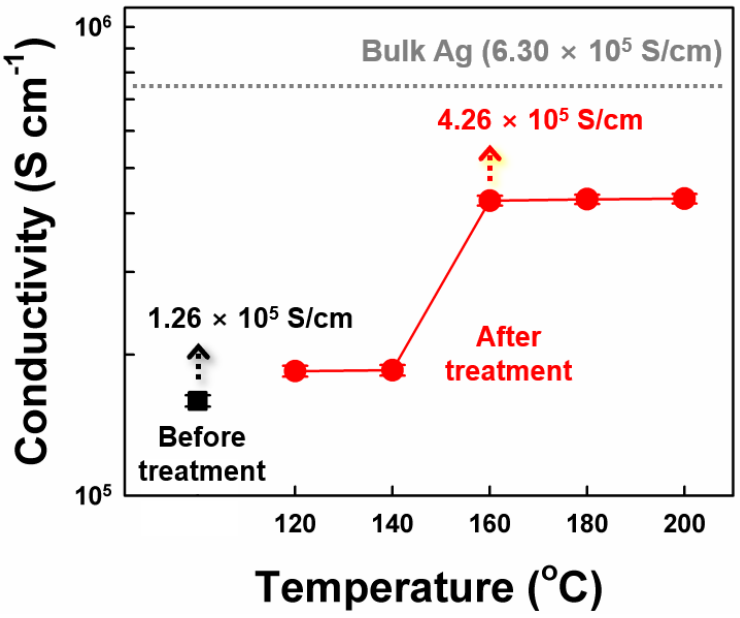

Figure S8. Electrical conductivity of (TOAS-Ag NP/TAA)$_{20}$ multilayers as a function of annealing temperature.

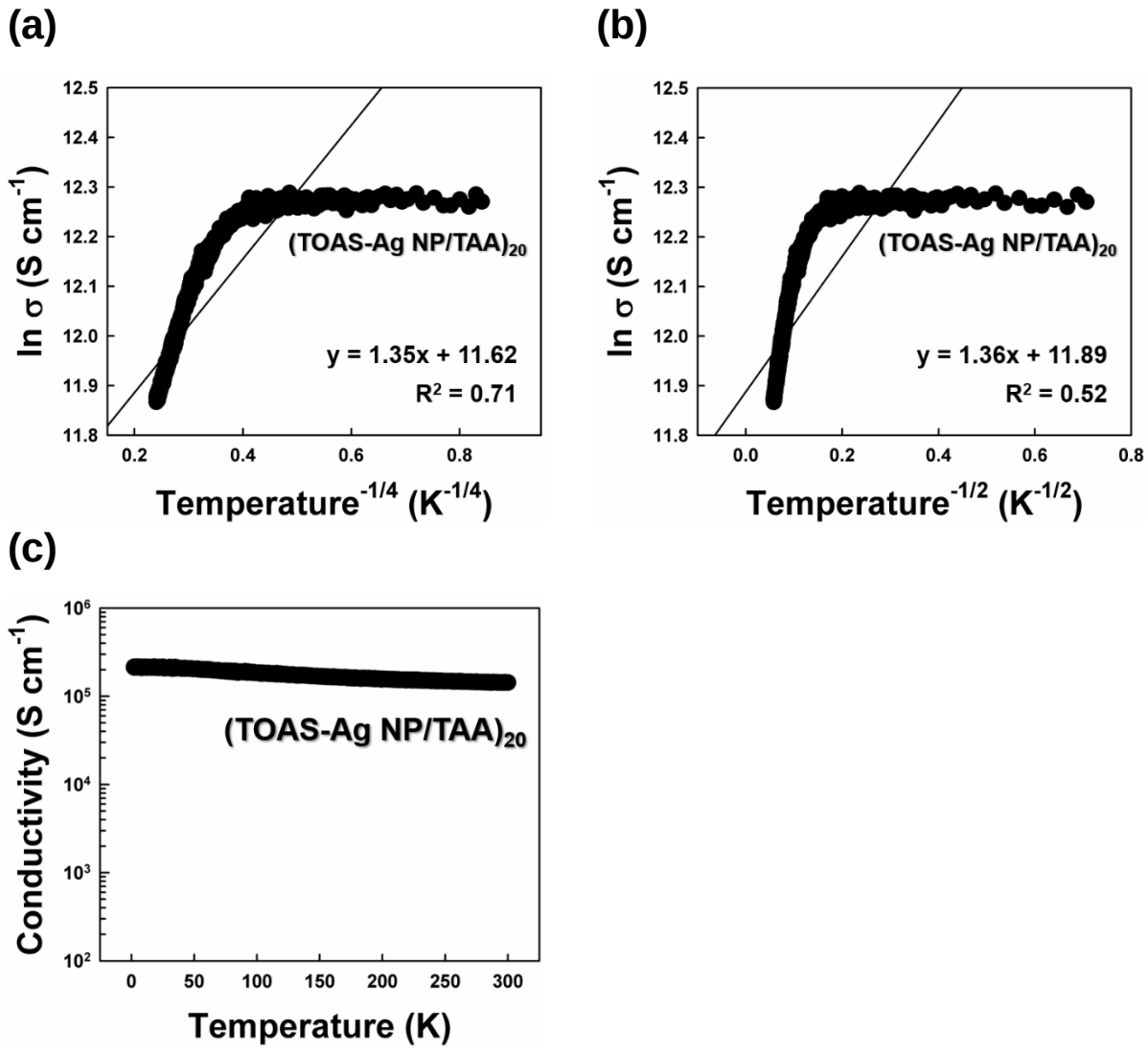

Figure S9. a) ln σ vs $T^{-1/4}$ plot for variable-range hopping (VRH) mechanism and b) ln σ vs $T^{-1/2}$ plot for tunneling mechanism of (TOAS-Ag NP/TAA)$_{20}$ multilayers from 2 to 300 K. Electron transport mechanism of VRH and tunneling conduction processes in a semiconductor can be described using the equation $\sigma = \sigma_0 \exp(-A/T^{(1/1+d)})$, where σ is the electrical conductivity, T is the absolute temperature [K], A is the constant, and d is the dimensionality. Here, d is 3 for VRH and is 1 for tunneling mechanism. As shown in figure S9a and S9b, (TOAS-Ag NP/TAA)$_n$ multilayers did not follow the semiconductor conduction behavior (two diagonal lines in graphs). c) Electrical conductivity of (TOAS-Ag NP/TAA)$_{20}$ multilayers as a function of temperature over the range from 2 to 300 K.

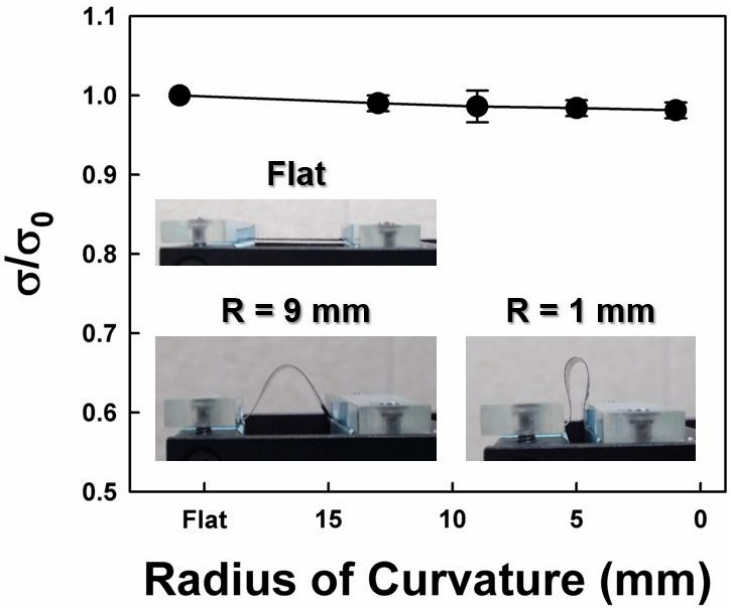

Figure S10. Electrical stability of (TOAS-Ag NP/TAA)$_{10}$ multilayer-coated PET substrate as a function of bending radius. The Ag NP-coated PET maintained 98.0% of its initial electrical conductivity ($\sigma_0 \sim 1.30 \times 10^5$ S cm^{-1}) under the bending radius of 1 mm.

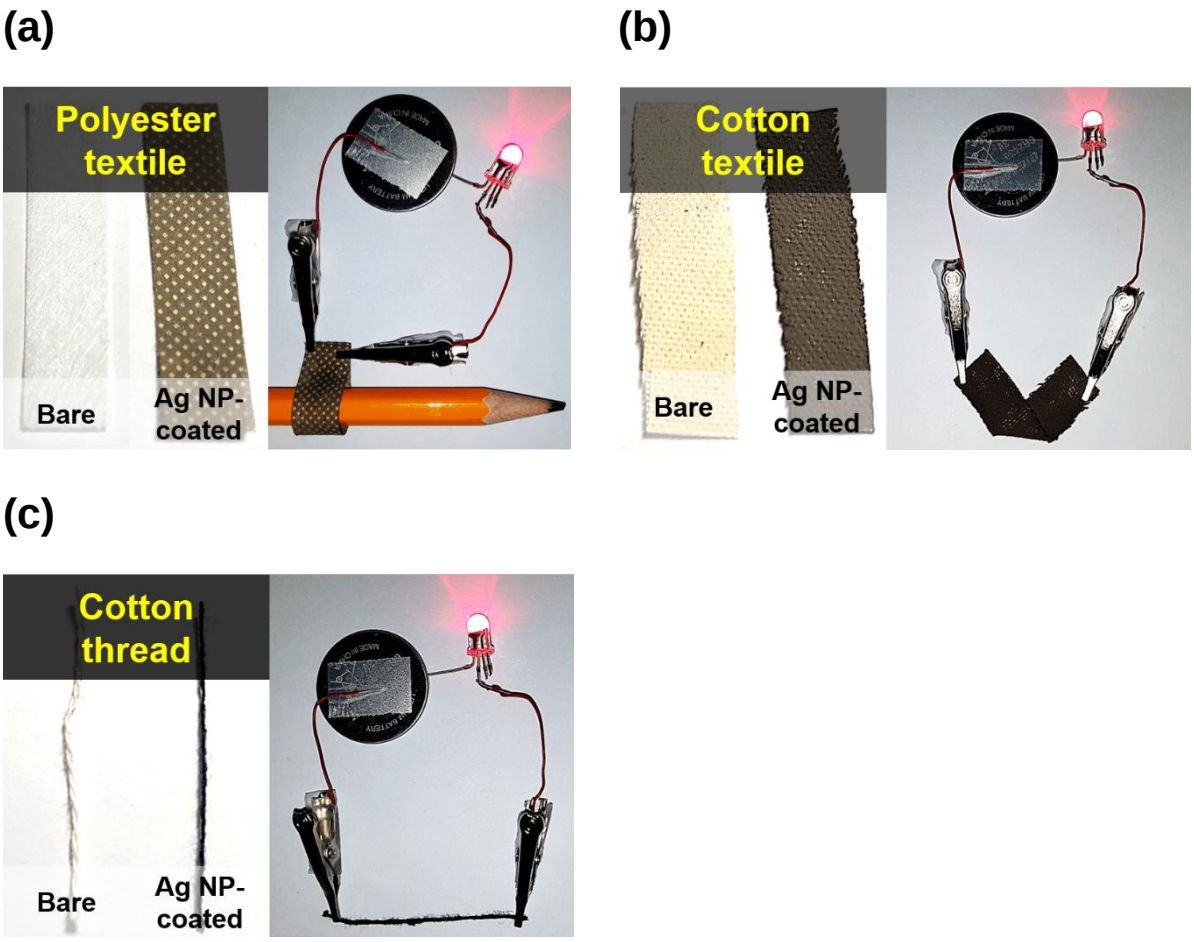

Figure S11. a) Metallic polyester textile, b) metallic cotton textile, and c) metallic cotton thread prepared by depositing (TOAS-Ag NP/TAA)$_{30}$ multilayers onto the substrates. These show that various materials of substrates regardless of size and shape can be coated with Ag NPs through our approach.

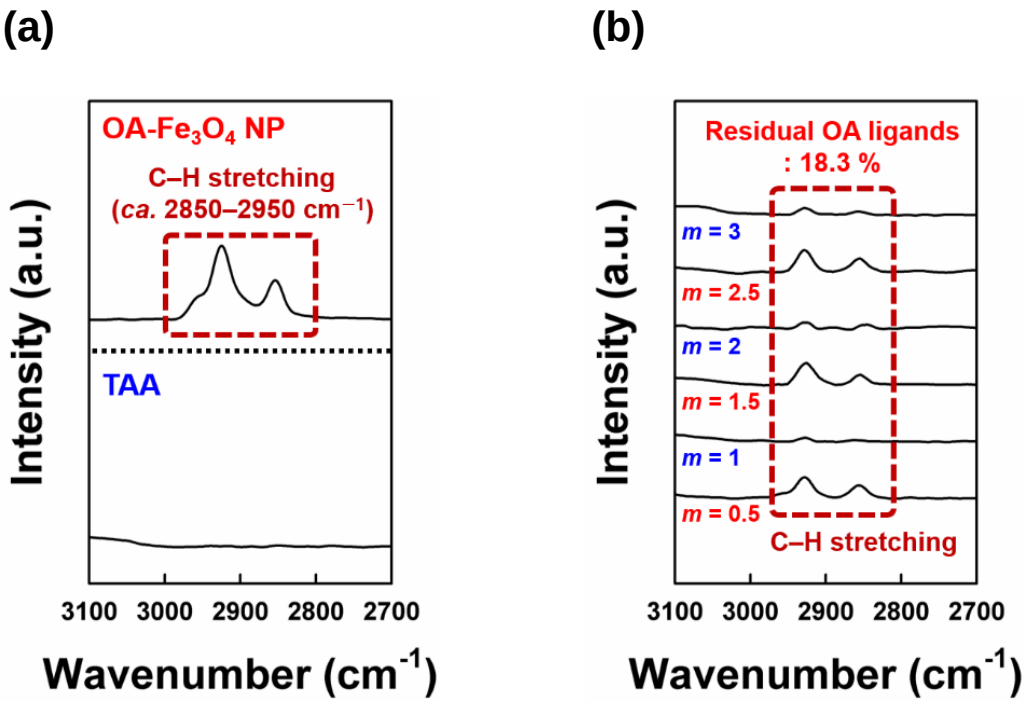

Figure S12. a) FTIR spectra of OA-Fe_3O_4 NPs and TAA. b) FTIR spectra of LbL-assembled (OA-Fe_3O_4 NP/TAA)$_m$ multilayers during a partial ligand-exchange reaction as a function of bilayer number (m). The persistent C−H stretching peaks (*ca.* 2850−2950 cm^{-1}) assigned to the long alkyl chains of OA ligands demonstrate that the deposition of TAA on the Fe_3O_4 NP layer-coated substrate partially removed the OA ligands loosely bound to Fe_3O_4 NP surface. These phenomena occurred because the electron-donating primary amine groups of TAA had a higher affinity for Fe_3O_4 NP surface than the carboxylate groups of OA ligand. The residual amount of OA ligands was 18.3% of the initial amount. Therefore, the C−H stretching peaks were generated and disappeared repeatedly by the alternative deposition of TAA and OA-Fe_3O_4 NPs.

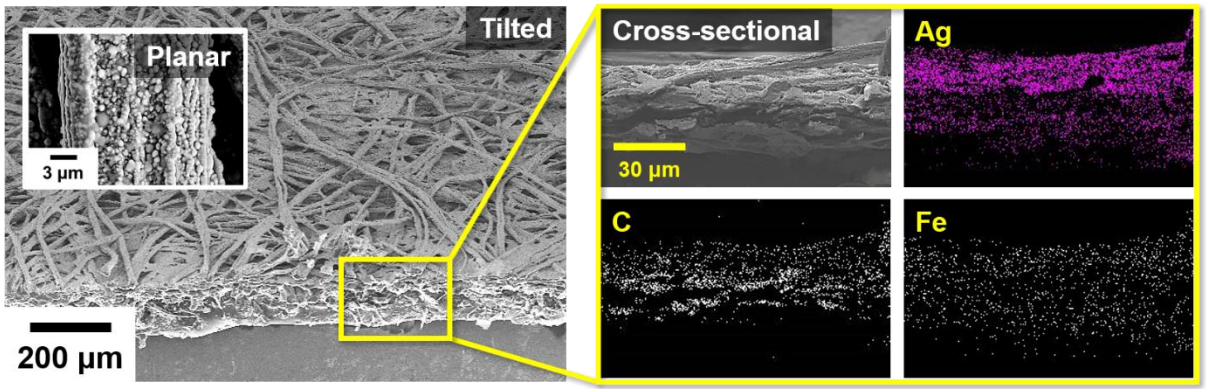

Figure S13. Planar, tilted, cross-sectional FE-SEM images and EDX images of Fe_3O_4-MCP electrode. In this case, Ag NPs and Fe_3O_4 NPs were densely packed onto cellulose fibers, maintaining the highly porous structure of the paper.

(a)

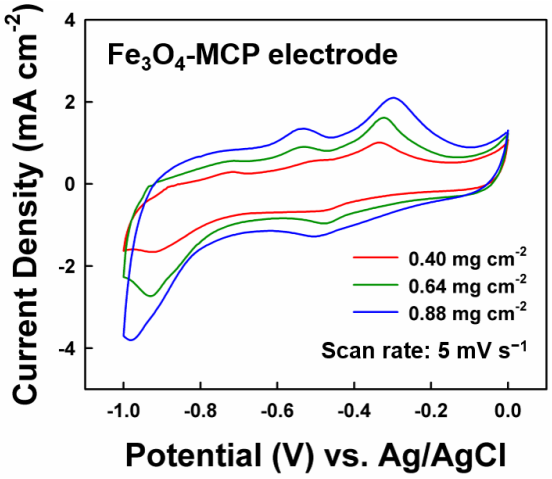
Fe3O4-MCP electrode
Current Density (mA cm-2)
Potential (V) vs. Ag/AgCl
0.40 mg cm-2
0.64 mg cm-2
0.88 mg cm-2
Scan rate: 5 mV s-1

(b)

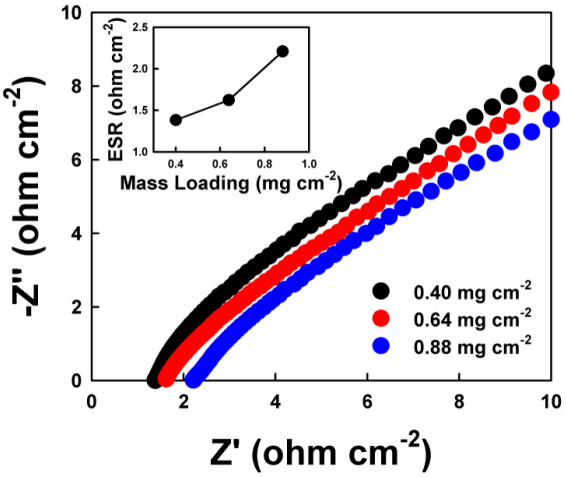
-Z'' (ohm cm-2)
Z' (ohm cm-2)
ESR (ohm cm-2)
Mass Loading (mg cm-2)
0.40 mg cm-2
0.64 mg cm-2
0.88 mg cm-2

(c)

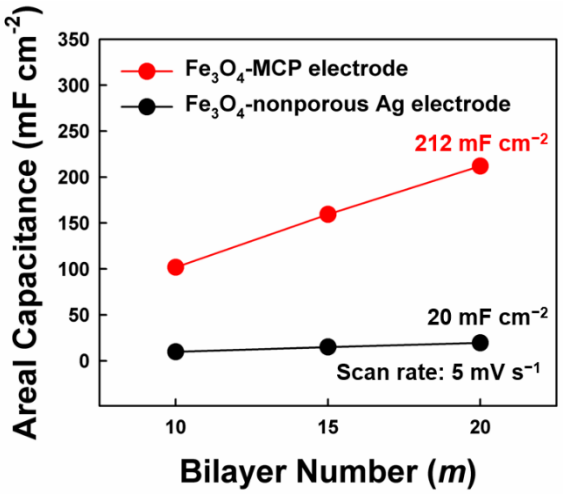
Areal Capacitance (mF cm-2)
Bilayer Number (m)
Fe3O4-MCP electrode
Fe3O4-nonporous Ag electrode
212 mF cm-2
20 mF cm-2
Scan rate: 5 mV s-1

(d)

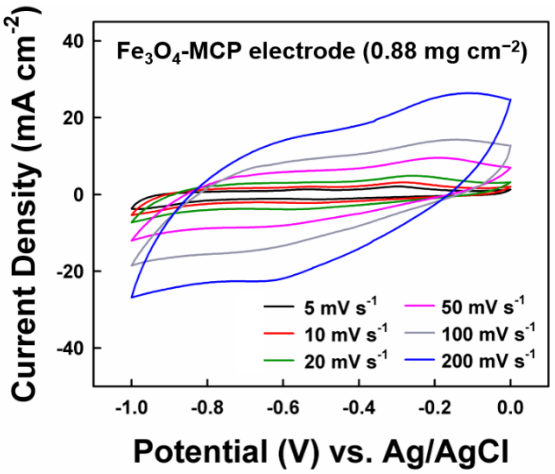
Fe3O4-MCP electrode (0.88 mg cm-2)
Current Density (mA cm-2)
Potential (V) vs. Ag/AgCl
5 mV s-1
10 mV s-1
20 mV s-1
50 mV s-1
100 mV s-1
200 mV s-1

(e)

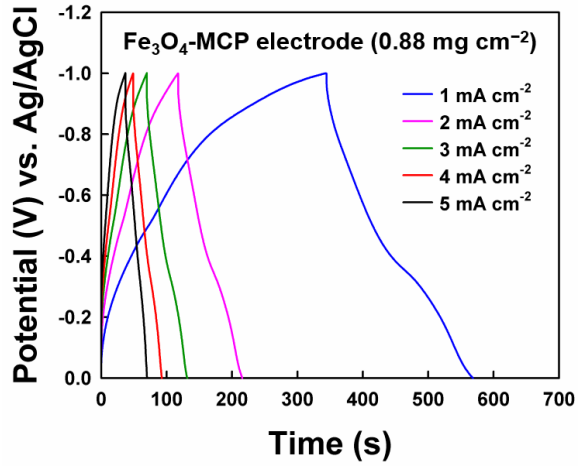
Fe3O4-MCP electrode (0.88 mg cm-2)
Potential (V) vs. Ag/AgCl
Time (s)
1 mA cm-2
2 mA cm-2
3 mA cm-2
4 mA cm-2
5 mA cm-2

Figure S14. a) Cyclic voltammograms of Fe_3O_4-MCP electrodes with increasing OA-Fe_3O_4 NP mass loading from 0.40 to 0.88 mg cm^{-2} at a scan rate of 5 mV s^{-1}. b) Nyquist plots and equivalent series resistance (ESR, inset) of Fe_3O_4-MCP electrodes as a function of mass loading. The value of ESR increased with increasing OA-Fe_3O_4 NP mass loading, which is the general tendency in pseudocapacitive materials-based electrodes.[S2] c) Areal capacitances of Fe_3O_4-MCP electrodes and Fe_3O_4-nonporous Ag electrodes as a function of bilayer number (m = 10, 15, and 20) at a scan rate of 5 mV s^{-1}. d) Cyclic voltammograms of Fe_3O_4-MCP electrodes with a mass loading of 0.88 mg cm^{-2} in a scan rate ranging from 5 to 200 mV s^{-1}. e) Galvanostatic charge/discharge (GCD) curves of Fe_3O_4-MCP electrodes with a mass loading of 0.88 mg cm^{-2} for current densities ranging from 1 to 5 mA cm^{-2}.

Table S1. Electrical conductivity comparison of Ag NP-based films.

Ag NPs	Fabrication methods Substrates	Additional treatments (Sintering principles)	Electrical conductivity [S cm^{-1}]	Ref.
TOAS-Ag NPs	**Metallic fusion-induced LbL assembly Various substrates (Glass, Si wafer, PET, paper)**	-	**1.60×10^5 (465 nm thickness)**	**Our work**
TOAS-Ag NPs	**Metallic fusion-induced LbL assembly Various substrates (Glass, Si wafer, paper)**	**Thermal annealing (160 ºC)**	**4.62×10^5 (313 nm thickness)**	**Our Work**
Alkylamine-stabilized Ag NPs	Spin-coating Glass	Thermal annealing (120 − 160 ºC)	$2.00 - 4.00 \times 10^4$ (70 nm thickness)	S3
Oleic acid-stabilized Ag NPs	Spin-coating Glass	Thermal annealing (200 ºC)	$2.00 - 4.00 \times 10^4$ (70 nm thickness)	S4
Dodecylamine-stabilized Ag NPs	Aerosol-jet printing PI[a] and paper	Thermal annealing (300 ºC)	6.30×10^4	S5
PVP[b]-stabilized Ag NPs	Inkjet printing Glass and PET	Self-aggregation after solvent evaporation	7.00×10^4 (400 nm thickness)	S6

PAA[c)]-stabilized Ag NPs	Inkjet printing Glass, PET, and paper	Charge neutralization by PDAC[d)]	1.26×10^5 (500 nm thickness)	S7
PAA-stabilized Ag NPs	Inkjet printing PET	Electrolyte treatments (*e.g.*, NaCl etc.)	2.58×10^5	S8
Ag NPs	Electroless plating Glass, Si wafer, PP[e)], PET, PMMA[f)], and PTFE[g)]	Electrolyte treatments (*e.g.*, $CaCl_2$ etc.)	$\sim 5.53 \times 10^4$ (~ 270 nm thickness)	S9**
Trioctylamine-stabilized Ag NPs	Spin-coating Glass and Si wafer	Ammonium thiocyanate treatment	1.14×10^5 (220 nm thickness)	S10
PAA-stabilized Ag NPs	Inkjet printing PET and PEN[h)]	Ar plasma & microwave treatment	3.78×10^5 (~ 250 nm thickness)	S11

[a)]PI: polyimide; [b)]PVP: poly(vinylpyrrolidone); [c)] PAA: poly(acrylic acid); [d)]PDAC: poly(diallyldimethylammonium chloride); [e)]PP: polypropylene; [f)]PMMA: poly(methyl methacrylate); [g)]PTFE: poly(tetrafluoroethylene); [h)]PEN: polyethylene naphthalate

** Electrical conductivity was evaluated from given data in the literature.

Supplementary References

[S1] R. McCaffrey, H. Long, Y. Jin, A. Sanders, W. Park, W. Zhang, *J. Am. Chem. Soc.* **2014**, *136*, 1782.

[S2] Y. He, W. Chen, X. Li, Z. Zhang, J. Fu, C. Zhao, E. Xie, *ACS Nano* **2013**, *7*, 174.

[S3] Y. Li, Y. Wu, B. S. Ong, *J. Am. Chem. Soc.* **2005**, *127*, 3266.

[S4] Y. Wu, Y. Li, B. S. Ong, *J. Am. Chem. Soc.* **2006**, *128*, 4202.

[S5] R. Shankar, L. Groven, A. Amert, K. W. Whites, J. J. Kellar, *J. Mater. Chem.* **2011**, *21*, 10871.

[S6] L. Polavarapu, K. K. Manga, H. D. Cao, K. P. Loh, Q.-H. Xu, *Chem. Mater.* **2011**, *23*, 3273.

[S7] S. Magdassi, M. Grouchko, O. Berezin, A. Kamyshny, *ACS Nano* **2010**, *4*, 1943.

[S8] M. Grouchko, A. Kamyshny, C. F. Mihailescu, D. F. Anghel, S. Magdassi, *ACS Nano* **2011**, *4*, 3354.

[S9] Y. Long, J. Wu, H. Wang, X. Zhang, N. Zhao, J. Xu, *J. Mater. Chem.* **2011**, *21*, 4875.

[S10] A. T. Fafarman, S.-H. Hong, S. J. Oh, H. Caglayan, X. Ye, B. T. Diroll, N. Engheta, C. B. Murray, C. R. Kagan, *ACS Nano* **2014**, *8*, 2746.

[S11] J. Perelaer, R. Jani, M. Grouchko, A. Kamyshny, S. Magdassi, U. S. Schubert, *Adv. Mater.* **2012**, *24*, 3993.